An Indoor Environment Sensing and Localization System via mmWave Phased Array

Yifei Sun, Jie Li, Tong Zhang, Rui Wang, Xiaohui Peng, Xiao Han, Haisheng Tan

***Abstract*—In this paper, an indoor layout sensing and localization system with testbed in the 60-GHz millimeter wave (mmWave) band, named mmReality, is elaborated. The mmReality system consists of one transmitter and one mobile receiver, both with a phased array and a single radio frequency (RF) chain. To reconstruct the room layout, the pilot signal is delivered from the transmitter to the receiver via different pairs of transmission and receiving beams, so that multipath signals in all directions can be captured. Then spatial smoothing and the two-dimensional multiple signal classification (MUSIC) algorithm are applied to detect the angle-of-departures (AoDs) and angle-of-arrivals (AoAs) of propagation paths. Moreover, the technique of multi-carrier ranging is adopted to measure the path lengths. Therefore, with the measurements of the receiver in different locations of the room, the receiver and virtual transmitters can be pinpointed to reconstruct the room layout. Experiments show that the reconstructed room layout can be utilized to localize a mobile device via the AoA spectrum.**

***Keywords*—millimeter wave, indoor sensing and localization, MUSIC algorithm, multi-input multi output (MIMO), room layout, integrated sensing and communication (ISAC), environment sensing, orthogonal frequency division multiplexing (OFDM)**

Manuscript received Sep. 20, 2022; revised Oct. 13, 2022; accepted Nov. 13, 2022. This work was supported by the National Natural Science Foundation of China under Grant 62171213. The associate editor coordinating the review of this paper and approving it for publication was X. Cheng.

Y. F. Sun, J. Li, T. Zhang, R. Wang. Department of Electronic and Electrical Engineering, Southern University of Science and Technology, Shenzhen 518055, China (e-mail: sunyf2019@mail.sustech.edu.cn; lij2019@mail.sustech.edu.cn; zhangt7@sustech.edu.cn; wang.r@sustech.edu.cn).

Y. F. Sun. Department of Computer Science, the University of Hong Kong, Hong Kong 999077, China (e-mail: sunyf2019@mail.sustech.edu.cn).

X. H. Peng, X. Han. Huawei Technologies Co., Ltd., Shenzhen 518129, China (e-mail: pengxiaohui5@huawei.com; tony.hanxiao@huawei.com).

H. S. Tan. LINKE Lab, School of Computer Science and Technology, the University of Science and Technology of China, Hefei 230026, China (e-mail: hstan@ustc.edu.cn).

I. Introduction

Millimeter wave (mmWave) communications have been one of the key technologies of next-generation wireless networks. Despite the large bandwidth, high propagation attenuation and reflection loss of mmWave signals are the drawbacks from the communication point of view. However, these drawbacks may favor the wireless sensing performance by degrading the interference. Hence, it is of interest to exploit the sensing capability of the mmWave communication system, such that the link reliability can be improved. For example, with the location knowledge of reflectors and mobile devices, the mmWave link can be quickly recovered if link blockage occurs.

There have been a few testbeds in the existing literature designated to detect the room layout via mmWave transceiver. For example in Ref. [1], co-located mmWave transmitter and receiver were deployed at a mobile platform to detect the layout of a corridor along a planned trajectory. In Ref. [2], an mmWave indoor mapping system with co-located transceiver was proposed, which utilized orthogonal frequency division multiplexing (OFDM) radar processing to obtain sparse range-angle charts. However, the above designs may not be applicable in a wireless communication system, where the signal transmitter and receiver are separated. Moreover, the self-interference cancellation for co-located transmitter and receiver is still challenging in communication systems. It was shown in Ref. [3] that indoor ambient reflectors can be detected via the mmWave transmitter and receiver, where the transmitter is fixed and the receiver receives signals at multiple locations. In this testbed, an omnidirectional antenna on a rotation platform is used to simulate an antenna array, such that angle-of-departures (AoDs) and angle-of-arrivals (AoAs) of the propagation paths can be estimated. Moreover, based on the detected layout, the distribution of the signal to noise ratio (SNR) in the room (radio map) is also predictable. However, it is more practical to use the phased array in mmWave communication systems, where imperfect antenna elements in the phased array may degrade the estimation accuracy of AoDs and AoAs.

To quickly recover mmWave communications from link

blockage, it is necessary for the access point (AP) to know both the room layout and the location of the mobile device. The localization methods in the existing literature can be classified into four categories, namely fingerprint-based localization, angle-based localization, time-of-flight-based (ToF-based) localization, and multipath-based localization, which are elaborated below.

Fingerprint-based localization: Localization based on fingerprints of received signal strength indicator (RSSI)[4,5] and channel state information (CSI)[6] has been well investigated in sub-6-GHz Wi-Fi networks. For example, RADAR[4] implemented a fingerprint-based localization system based on an offline RSSI database. In Ref. [5], a probabilistic method was proposed to improve RSSI-fingerprint-based localization. DeepFi[6] adopted CSI as the fingerprint for deep-learning-based indoor localization. In the mmWave band, instead of using fine-grained CSI or coarse-grained RSSI as the fingerprint, mid-grained beam SNR was chosen as the fingerprint in Ref. [7]. However, the fingerprint-based localization method is vulnerable to a rich multipath environment. Moreover, since the fingerprints should be updated when the environment changes, collecting fingerprints at many locations could be labor-intensive.

Angle-based localization: The AoDs and AoAs of multipath can be estimated by the multiple signal classification (MUSIC) algorithm when the devices are equipped with antenna arrays. In Ref. [8], ArrayTrack estimated the AoA spectra of multiple APs from the uplink signals of the device and then generated the localization likelihood heatmap. SpotFi[9] utilized the AoA estimated by MUSIC algorithm and ToF estimated from OFDM subcarriers of direct paths to localize the target with three-antenna APs. Phaser[10] addressed the practical problems of AoA-based localization such as auto-calibration and multi-AP synchronization in commodity Wi-Fi APs. However, these angle-based localization systems required multiple APs. Moreover, they applied MUSIC-based algorithms on digital multi-input multi-output (MIMO) architecture, while the analog MIMO architecture is widely used in mmWave systems. The angle estimation methods used in these sub-6-GHz systems cannot be directly applied to mmWave systems.

ToF-based localization: Chronos[11] estimated accurate ToFs of multipath by hopping between different bands. Then ToF of the line-of-sight (LoS) path was distinguished from non-line-of-sight (NLoS) paths for accurate localization. However, such frequency hopping will degrade the throughputs of other devices. ToneTrack[12] proposed a spectrum identification algorithm to discard NLoS measurement. It requested time synchronization between the transmitter and the receiver for accurate ToF estimation, and the LoS path was required for high-accuracy localization. However, the localization error might be significant when applying the ToF-based method in mmWave communication systems. This is because of the severe and time-varying carrier frequency offset between the transmitter and the receiver.

Multipath-based localization: Angle-based and ToF-based localization methods generally request multiple APs for triangular and trilateral localization. In Ref. [13], the authors combined the azimuth angles and relative ToFs of multipaths of a single AP for localization. MonoLoco[14] proposed a multipath triangulation method to achieve decimeter-level Wi-Fi localization with a single AP. However, these methods still suffer from the frequency offset as the ToF-based localization in the mmWave band. As a result, the existing localization methods for sub-6-GHz systems may not be directly applicable to mmWave systems. Furthermore, although the room layout and device location are strongly related, there is no existing work integrating the layout reconstruction and localization in mmWave communication systems.

In this paper, an indoor sensing and localization system working at 60 GHz, namely mmReality, is proposed. The mmReality consists of one transmitter and one receiver, each with one phased array. The system works in two stages, namely the layout reconstruction stage and the localization stage. In the first stage, the AoAs, AoDs, and lengths of the propagation paths between the transmitter and the receiver are estimated, where the receiver is put in multiple positions. Based on the above geometric parameters, the walls of the room can be detected to reconstruct the layout. In the second stage, the AoA spectrum for each indoor position can be predicted via the room layout, and the position of a mobile device can be detected by comparing its AoA spectrum with the prediction.

The remainder of this paper is organized as follows. In section II, the architecture of the mmReality is introduced. In section III, the estimation methods for AoAs, AoDs, and lengths of propagation paths are elaborated, and the algorithms for layout reconstruction are elaborated in section IV. Then section V describes the localization method based on room layout and AoA spectrum. Finally, the experimental results are illustrated in section VI and the conclusion is drawn in section VII.

II. System Overview

The proposed mmReality system consists of one transmitter at a fixed location in a room and one mobile receiver, each with a single radio frequency (RF) chain and a phased array working at 60 GHz. There are N_{T} transmit antenna elements (TAEs) and N_{R} receive antenna elements (RAEs) in the phased arrays of the transmitter and receiver, respectively. The propagation paths from the transmitter to the receiver, including the LoS and NLoS paths, are illustrated in Fig. 1, where the specular reflections via walls dominate the NLoS paths. By

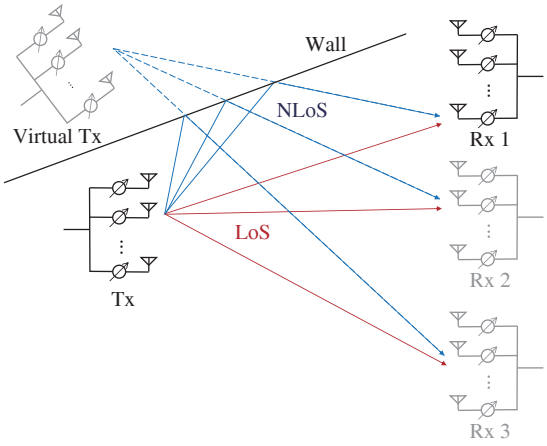

Fig. 1 Illustration of propagation channel between the transmitter and the receiver, where the transmitter is fixed and a virtual transmitter can be observed by the receiver due to the specular reflection of the wall

measuring the multi-carrier pilot signals with the phased array, the transmitter and receiver can cooperatively estimate the AoDs, AoAs, and lengths of propagation paths. Hence, the relative locations of the main reflectors (e.g., walls) and the mobile receiver with respect to the transmitter can be detected via geometric relations. The receiver moves according to the planned trajectory in the room so that a complete room layout can be reconstructed. In practice, the transmitter can also communicate with multiple receivers at different locations in the room to complete the layout detection. In the following section III, we first introduce how to estimate AoDs, AoAs, and path lengths, then the layout reconstruction algorithm will be elaborated in section IV.

III. Estimation of AoD, AoA, and Path Length

A. Joint AoD and AoA Estimation

The detection of AoD and AoA is challenging with analog MIMO architecture. For example, the exhaustive beam search used in Ref. [2] is with high estimation overhead and low angular resolution. Although there has been a significant amount of research efforts spent on angle detection in multi-antenna systems, e.g., MUSIC algorithm and estimating signal parameter via rotational invariance techniques (ESPRIT) algorithm, they are designed for digital MIMO systems, where the signals at all the antenna elements can be sampled individually. Notice that in the scenario of sensing a room layout, the main reflectors (e.g., walls) are static. Therefore, the mmWave channel can be treated as quasi-static during multiple transmissions. This has been verified and utilized in Ref. [3] for AoD and AoA detection with a single rotating antenna. In this paper, exploiting this phenomenon, the transmitter can duplicate pilot transmissions via the same transmission beams while the receiver adopts different receiving beams to resolve the individual signal on each RAE.

Specifically, the pilot signal $s[t]$ ($t=1,2,\cdots,N_{\mathrm{S}}$) is periodically transmitted via N_{T} different analog precoders, namely $\{\boldsymbol{f}_1,\boldsymbol{f}_2,\cdots,\boldsymbol{f}_{N_{\mathrm{T}}}\}$, where N_{S} is the number of symbols in the transmission signal. For each analog precoder, the signal $s[t]$ is transmitted N_{R} times, while N_{R} different analog combiners are used at the receiver, namely $\{\boldsymbol{w}_1,\boldsymbol{w}_2,\cdots,\boldsymbol{w}_{N_{\mathrm{R}}}\}$. For the elaboration convenience, we refer to the transmission with the ith precoder and jth combiner as the (i,j)th transmission. The received signal of the (i,j)th transmission can be expressed as

$$\tilde{y}_{i,j}[t] = \boldsymbol{w}_j^{\mathrm{H}}\boldsymbol{H}\boldsymbol{f}_i s[t]+n[t]= \tag{1}$$

$$\boldsymbol{w}_j^{\mathrm{H}}\boldsymbol{S}[t]\boldsymbol{f}_i+n[t], \tag{2}$$

where $\boldsymbol{w}_j^{\mathrm{H}}$ denotes the conjugate transpose of the jth combiner $\boldsymbol{w}_j$, $\boldsymbol{H}$ denotes the channel matrix, $n[t]$ denotes the additive white Gaussian noise, and

$$\boldsymbol{S}[t]=\boldsymbol{H}s[t]\in\mathbb{C}^{N_{\mathrm{R}}\times N_{\mathrm{T}}} \tag{3}$$

denotes the TAE-to-RAE signal matrix. Aggregating the transmissions via all the precoder and combiner pairs, we have

$$\widetilde{\boldsymbol{Y}}[t]=\boldsymbol{W}^{\mathrm{H}}\boldsymbol{S}[t]\boldsymbol{F}+\boldsymbol{N}[t], \tag{4}$$

where the (i,j)th entry of matrix $\widetilde{\boldsymbol{Y}}[t]$ is the received signal when applying the ith precoder and the jth combiner $\tilde{y}_{i,j}[t]$, $\boldsymbol{F}=[\boldsymbol{f}_1,\boldsymbol{f}_2,\cdots,\boldsymbol{f}_{N_{\mathrm{T}}}]$, $\boldsymbol{W}=[\boldsymbol{w}_1,\boldsymbol{w}_2,\cdots,\boldsymbol{w}_{N_{\mathrm{R}}}]$, and $\boldsymbol{N}[t]$ is the aggregation of noise in all the transmissions. Applying the unitary beamforming matrix proposed in Ref. [15], we have $\boldsymbol{F}^{\mathrm{H}}\boldsymbol{F}=\boldsymbol{I}$ and $\boldsymbol{W}^{\mathrm{H}}\boldsymbol{W}=\boldsymbol{I}$. As a result, the signal matrix $\boldsymbol{S}[t]$ can be estimated from received signals $\widetilde{\boldsymbol{Y}}(t)$ by

$$\widehat{\boldsymbol{S}}[t]=\boldsymbol{W}\widetilde{\boldsymbol{Y}}[t]\boldsymbol{F}^{\mathrm{H}}, \tag{5}$$

where $\widehat{\boldsymbol{S}}[t]$ denotes the estimation of $\boldsymbol{S}[t]$.

Two-dimensional-MUSIC (2D-MUSIC) algorithm with spatial smoothing is used for AoD and AoA estimation from $\widehat{\boldsymbol{S}}[t]$. Although the spatial smoothing may lose some degree of freedom in the angle detection, it significantly suppresses the detection error due to source correlation[16]. In order to proceed the spatial smoothing with subarray sizes N'_{T} and N'_{R} at the transmitter and receiver respectively, we first define $\widehat{\boldsymbol{S}}_{i,j}[t]$ as the submatrix of $\boldsymbol{S}[t]$ by extracting the entries from the ith row to $(i+N'_{\mathrm{T}}-1)$th row and from the jth column to $(j+N'_{\mathrm{R}}-1)$th column, and $\widehat{\boldsymbol{s}}_{\mathrm{v}}^{i,j}[t]$ as the vectorization of $\widehat{\boldsymbol{S}}_{i,j}[t]$. Hence, the covariance matrix of $\widehat{\boldsymbol{s}}_{\mathrm{v}}^{i,j}[t]$ is given by

$$\widehat{\boldsymbol{R}}_{i,j}=\frac{1}{T}\sum_{t=1}^{T}\widehat{\boldsymbol{s}}_{\mathrm{v}}^{i,j}[t]\left[\widehat{\boldsymbol{s}}_{\mathrm{v}}^{i,j}[t]\right]^{\mathrm{H}}, \tag{6}$$

where $[\widehat{\boldsymbol{s}}_{\mathrm{v}}^{i,j}[t]]^{\mathrm{H}}$ denotes the conjugate transpose of $\widehat{\boldsymbol{s}}_{\mathrm{v}}^{i,j}[t]$. Then the spatially smoothed covariance matrix is defined as

the average covariance matrix of each subarray,

$$\widehat{\boldsymbol{R}}_{\mathrm{ss}} = \frac{1}{M_{\mathrm{T}} M_{\mathrm{R}}} \sum_{i=1}^{M_{\mathrm{T}}} \sum_{j=1}^{M_{\mathrm{R}}} \widehat{\boldsymbol{R}}_{i,j}, \tag{7}$$

where $M_{\mathrm{T}} = N_{\mathrm{T}} - N'_{\mathrm{T}} + 1$ and $M_{\mathrm{R}} = N_{\mathrm{R}} - N'_{\mathrm{R}} + 1$. With the estimated path number K, $\widehat{\boldsymbol{R}}_{\mathrm{ss}}$ is further decomposed via eigenvalue decomposition as

$$\widehat{\boldsymbol{R}}_{\mathrm{ss}} = \boldsymbol{E}_{\mathrm{s}} \boldsymbol{D}_{\mathrm{s}} \boldsymbol{E}_{\mathrm{s}}^{\mathrm{H}} + \boldsymbol{E}_{\mathrm{n}} \boldsymbol{D}_{\mathrm{n}} \boldsymbol{E}_{\mathrm{n}}^{\mathrm{H}}, \tag{8}$$

where $\boldsymbol{D}_{\mathrm{s}}$ and $\boldsymbol{D}_{\mathrm{n}}$ are diagonal matrices whose diagonal entries are the K largest and the $(N'_{\mathrm{T}} N'_{\mathrm{R}} - K)$ smallest eigenvalues of $\widehat{\boldsymbol{R}}_{\mathrm{ss}}$, respectively; $\boldsymbol{E}_{\mathrm{s}}$ and $\boldsymbol{E}_{\mathrm{n}}$ are matrices composed of the eigenvectors of $\widehat{\boldsymbol{R}}_{\mathrm{ss}}$ correspondingly.

As a result, the 2D-MUSIC spatial spectrum function is given by

$$f(\phi, \theta) = \frac{1}{[\boldsymbol{a}_{\mathrm{R}}(\phi) \otimes \boldsymbol{a}_{\mathrm{T}}(\theta)]^{\mathrm{H}} \boldsymbol{E}_{\mathrm{n}} \boldsymbol{E}_{\mathrm{n}}^{\mathrm{H}} [\boldsymbol{a}_{\mathrm{R}}(\phi) \otimes \boldsymbol{a}_{\mathrm{T}}(\theta)]}, \tag{9}$$

where $\otimes$ denotes the Kronecker product,

$$\begin{aligned} \boldsymbol{a}_{\mathrm{T}}(\theta) &= \left[1, \mathrm{e}^{-\mathrm{j}2\pi \frac{d \sin\theta}{\lambda}}, \cdots, \mathrm{e}^{-\mathrm{j}2\pi \frac{(N'_{\mathrm{T}}-1) d \sin\theta}{\lambda}}\right]^{\mathrm{T}}, \\ \boldsymbol{a}_{\mathrm{R}}(\phi) &= \left[1, \mathrm{e}^{-\mathrm{j}2\pi \frac{d \sin\phi}{\lambda}}, \cdots, \mathrm{e}^{-\mathrm{j}2\pi \frac{(N'_{\mathrm{R}}-1) d \sin\phi}{\lambda}}\right]^{\mathrm{T}} \end{aligned} \tag{10}$$

denote the transmission and receiving array response vectors, respectively. d, λ, and $\boldsymbol{x}^{\mathrm{T}}$ denote the inter-element spacing, the wavelength, and the transpose of vector $\boldsymbol{x}$, respectively. The K highest peaks of $f(\phi, \theta)$ refer to the estimated AoDs and AoAs of the propagation paths.

B. Path Length Estimation

With the knowledge of AoDs and AoAs of propagation paths, signals from different paths can be separated from $\widehat{\boldsymbol{S}}[t]$ via the transmission and receiving beamforming, so that the length of each path can be estimated individually. Specifically, the path length estimation of the ith path, whose AoD and AoA are denoted as θ_i and ϕ_i respectively, is elaborated below. Let $\boldsymbol{A}_{\mathrm{T},i}$ be the aggregation of transmission array response vectors of all AoDs with its first column as $\boldsymbol{a}(\phi_i)$, $\boldsymbol{A}_{\mathrm{R},i}$ be the aggregation of receiving array response vectors of all AoAs with its first column as $\boldsymbol{a}(\theta_i)$, $\boldsymbol{e}_{\mathrm{T},1} = [1, 0, \cdots, 0]^{\mathrm{T}} \in \{0,1\}^{N_{\mathrm{T}}}$ and $\boldsymbol{e}_{\mathrm{R},1} = [1, 0, \cdots, 0]^{\mathrm{T}} \in \{0,1\}^{N_{\mathrm{R}}}$, the transmission and the receiving beamforming vectors for the ith path are given by

$$\boldsymbol{a}_{\mathrm{T},i}^{\mathrm{null}} = (\boldsymbol{A}_{\mathrm{T},i} \boldsymbol{A}_{\mathrm{T},i}^{\mathrm{H}})^{-1} \boldsymbol{A}_{\mathrm{T},i} \boldsymbol{e}_{\mathrm{T},1}, \tag{11}$$

and

$$\boldsymbol{a}_{\mathrm{R},i}^{\mathrm{null}} = (\boldsymbol{A}_{\mathrm{R},i} \boldsymbol{A}_{\mathrm{R},i}^{\mathrm{H}})^{-1} \boldsymbol{A}_{\mathrm{R},i} \boldsymbol{e}_{\mathrm{R},1}, \tag{12}$$

respectively. The received signal of the ith path can be estimated as

$$s_i[t] = \boldsymbol{a}_{\mathrm{R},i}^{\mathrm{null}} \boldsymbol{S}(t) (\boldsymbol{a}_{\mathrm{T},i}^{\mathrm{null}})^{\mathrm{H}}. \tag{13}$$

OFDM ranging, also called multi-carrier ranging[11], is applied on $s_i[t]$ to estimate the length of the ith path. In the OFDM system, signals are modulated to subcarriers with different frequencies for transmission. For the same distance, the phases of the received signals of all subcarriers are different, which can be exploited to estimate the path lengths. We select equally-separated subcarriers for ranging. Without the consideration of sampling frequency offset (SFO) and packet detect delay, the estimated path length can be represented by

$$d^{\star} = \arg\max_{d} \left| \sum_{i=1}^{L} \exp\left(\mathrm{j}\left(\varphi_i - \frac{2\pi f_i d}{c}\right)\right) \right|, \tag{14}$$

where φ_i is the phase of the ith subcarrier, $\frac{2\pi f_i d}{c}$ denotes the range-dependent phase offset of the ith subcarrier, f_i denotes the frequency of the ith subcarrier, c denotes the speed of light, and L is the number of subcarriers. As a remark notice that, when d equals the ground truth, the range-dependent phase offsets of all subcarriers will be equal, i.e., their complex exponentials are in-phase.

In practice, however, the SFO and packet detect delay are not negligible[17]. As in Ref. [3], a reference calibration scheme can be used to address this issue. Suppose the measured phase is $\varphi_{i,\mathrm{ref}}$ for the ith subcarrier at a known distance d_0, (14) can be reformulated as

$$d^{\star} = \arg\max_{d} \left| \sum_{i=1}^{L} \exp\left(\mathrm{j}\left(\varphi_i - \varphi_{i,\mathrm{ref}} - \frac{2\pi f_i (d - d_0)}{c}\right)\right) \right|. \tag{15}$$

IV. Reconstruction of Room Layout

With the technique introduced in the previous section, the geometrical parameters of propagation paths, including AoAs, AoDs, and path lengths, can be estimated. In this section, following the method introduced in Ref. [3], we first localize the mobile receiver in each measurement (referred to as the measurement points) and then reconstruct the room layout.

A. Localization of Measurement Points

Since the magnetometer has been widely adopted in mobile devices, it is assumed that both the transmitter and receiver are able to share the same direction as the reference direction of AoA and AoD measurements. Moreover, the estimated geometrical parameters of paths are reported to the transmitter for the layout reconstruction. For the elaboration convenience, we treat the position of the transmitter as the origin of the coordinate system, define $\boldsymbol{p}_i^{\mathrm{rx}}$ as the coordinates of the ith measurement point, $\boldsymbol{p}_{i,\ell}^{\mathrm{ref}}$ as the coordinates of the reflection point of ℓth path at the ith measurement point. Moreover, tracing back the AoA of one NLoS path (say the ℓth path) from the ith measurement point, the receiver can find the mirror position

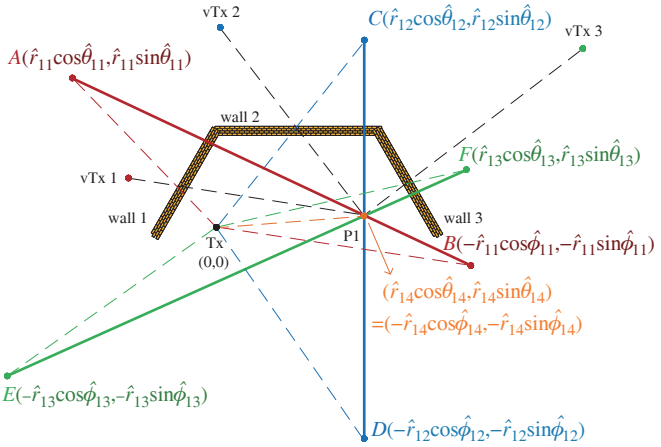

Fig. 2 Localization of a measurement point, where vTx refers to the virtual transmitter

of the transmitter (virtual transmitter[3]) with respect to a wall as illustrated in Fig. 1, which is denoted as $\boldsymbol{p}_{i,\ell}^{\mathrm{vtx}}$. For the elaboration convenience, we refer to the abovementioned mirror of transmitters as virtual transmitters. Suppose that there are L paths found at the ith measurement point $\boldsymbol{p}_i^{\mathrm{rx}}$, and the estimated AoA, AoD, and distance of the ℓth path ($\ell = 1,2,\cdots,L$) are $(\widehat{\theta}_{i,\ell},\widehat{\phi}_{i,\ell},\widehat{r}_{i,\ell})$. The detection of $\boldsymbol{p}_i^{\mathrm{rx}}$, denoted by $\widehat{\boldsymbol{p}}_i^{\mathrm{rx}}$ is elaborated below.

It can be proved that, without estimation error, the measurement point must be on the line segment with its two endpoints represented by $(\widehat{r}_{i,\ell}\cos\widehat{\theta}_{i,\ell},\widehat{r}_{i,\ell}\sin\widehat{\theta}_{i,\ell})$ and $(-\widehat{r}_{i,\ell}\cos\widehat{\phi}_{i,\ell},-\widehat{r}_{i,\ell}\sin\widehat{\phi}_{i,\ell})$, $(\ell = 1,2,\cdots,L)$. An example is illustrated in Fig. 2, where the measurement point P1 is on the line segment connecting $(\widehat{r}_{1,1}\cos\widehat{\theta}_{1,1},\widehat{r}_{1,1}\sin\widehat{\theta}_{1,1})$ and $(-\widehat{r}_{1,1}\cos\widehat{\phi}_{1,1},-\widehat{r}_{1,1}\sin\widehat{\phi}_{1,1})$, which are marked in red. Hence, as long as more than one path is detected in P1, its location can be estimated from the intersection points of corresponding line segments. In practice, due to the measurement error, the intersection points are not unique, then the measurement point can be estimated by finding a point $\widehat{\boldsymbol{p}}_i^{\mathrm{rx}} = (\widehat{x}_i^{\mathrm{rx}},\widehat{y}_i^{\mathrm{rx}})$ minimizing the sum distance to the line segments specified by all paths[3].

After pinpointing a measurement point, the estimated reflection points of the ℓth path ($\ell = 1,2,\cdots,L$), denoted as $\widehat{\boldsymbol{p}}_{i,\ell}^{\mathrm{ref}} = (\widehat{x}_{i,\ell}^{\mathrm{ref}},\widehat{y}_{i,\ell}^{\mathrm{ref}})$, can be calculated via the following equation system

$$\begin{cases} \dfrac{\widehat{x}_{i,\ell}^{\mathrm{ref}}}{\widehat{y}_{i,\ell}^{\mathrm{ref}}} = \tan\widehat{\theta}_{i,\ell}, \\ \dfrac{\widehat{x}_{i,\ell}^{\mathrm{ref}} - \widehat{x}_i^{\mathrm{rx}}}{\widehat{y}_{i,\ell}^{\mathrm{ref}} - \widehat{y}_i^{\mathrm{rx}}} = \tan\widehat{\phi}_{i,\ell}. \end{cases} \tag{16}$$

Moreover, the mirror position of the transmitter along the ℓth path at the ith measurement point can be estimated by

$$\widehat{\boldsymbol{p}}_{i,\ell}^{\mathrm{vtx}} = \widehat{\boldsymbol{p}}_i^{\mathrm{rx}} + \widehat{r}_{i,\ell}\left[\cos\widehat{\phi}_{i,\ell},\sin\widehat{\phi}_{i,\ell}\right]^{\mathrm{T}}. \tag{17}$$

As illustrated in the example of Fig. 2, there are three virtual transmitters from the P1 point of view. As a remark notice that the positions of virtual transmitters depend only on the position of the transmitter and the layout of walls, and hence, the receiver should see the same set of virtual transmitters at different measurement points.

B. Layout Reconstruction

It can be observed from Fig. 2 that, after the localization of virtual transmitters, the wall can be detected by drawing the perpendicular bisector between the transmitter and each virtual transmitter. To obtain the complete room layout, we can move the receiver and take measurements in a number of points, so that the virtual transmitters with respect to all the walls can be captured.

In real measurement, there are still two issues with the above reconstruction method. First, due to the measurement error, the estimated locations of one virtual transmitter detected at different measurement points may not be identical. Moreover, in addition to the first-order path (the path with one reflection from the transmitter to the receiver), some higher-order paths (the path with more than one reflection) may also be detected. As a result, the detected locations of virtual transmitters may be dispersed. To classify the estimated positions of virtual transmitters corresponding to the same wall, we use density-based spatial clustering of applications with noise (DBSCAN) method[18] and take the cluster centroid as the estimated position of the virtual transmitter.

Finally, for some complicated room layouts, there is more than one possible room layout given the locations of virtual transmitters. One example is illustrated in Fig. 3, where there are two possible layouts given the same locations of 6 virtual transmitters. This ambiguity can be removed by exploiting the locations of reflection points derived in (16). For example, in Fig. 3, if A and B are the reflection points of NLoS paths from vTx2 and vTx3 to the receivers respectively, then the room profile is shown in Fig. 3(a). Otherwise, if A' and B' are the reflection points, the room profile is shown in Fig. 3(b).

V. Localization by AoA Spectrum

In this section, the fast localization method for mobile receivers via AoA spectrum and reconstructed indoor layout is explained. Although the method introduced in section IV.A can be used to localize the receiver, the overhead is significant. First, the transmitter should deliver pilots dedicatedly to the receiver for at least $N_{\mathrm{T}}N_{\mathrm{R}}$ times, such that the AoA and AoD can be estimated with high resolution. However, this estimation method may not be feasible when the channel is not quasi-static, e.g., there are moving persons in the room. Second, the offset between their local oscillators should be carefully calibrated to suppress the estimation error of path

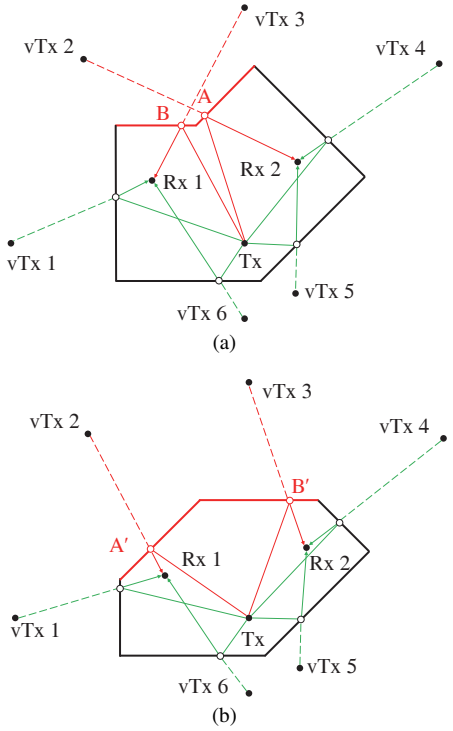

Fig. 3 Two possible layouts with the same virtual transmitter positions due to layout ambiguity: (a) Layout with reflection points A and B; (b) Layout with reflection points A' and B'

length. The cost of oscillator synchronization could be high, especially in the mmWave band.

In practice, the transmitter (i.e., the AP) would periodically broadcast control information to all directions, so that each receiver can detect all the potential AoAs of the signals from the transmitter via periodic beam search. Hence, raw AoA estimation can be made by the receiver. By matching the observed dominant AoAs with the locations in the reconstructed room layout, the mobile receiver can be pinpointed. This facilitates localization without dedicated signaling overhead. The existing works exploiting the AoA spectrum (including the AoAs and signal powers at the arrival directions) in localization usually rely on multiple APs. Compared with the existing works in sub-6-GHz, we shall show single transmitter might be sufficient to generate the AoA spectrum for localization in the mmWave band, with the assistance of virtual transmitters. The reasons are elaborated on below. First, it is shown by experiments that the propagation paths arrived at the receiver are dominated by the LoS and first-order NLoS paths, leading to the limited number of virtual transmitters. Second, the phased array at the mmWave band is of smaller size, so that it can be implemented on mobile devices, and used to resolve the real and virtual transmitters in different directions.

Specifically, we choose $|\mathscr{G}|$ positions as the possible position in the reconstructed room layout, denoted as $\mathscr{G} = \{1,2,\cdots,|\mathscr{G}|\}$. In practice, the set of the feasible positions $\mathscr{G}$ can be generated by mesh grids. Then the expected AoA spectra at all positions in $\mathscr{G}$ is calculated according to the positions of the transmitter and virtual transmitters. Let $\Phi_i = \{\phi_{i,j}|j=1,2,\cdots\}$ be the set of AoAs for the position i, and $\widehat{\Phi}$ be the set of AoAs observed at the real receiver. We define the error function of an expected AoA profile with respect to the measured one as

$$f(\Phi_i,\widehat{\Phi}) = \sum_{j=1}^{|\Phi_i|} \min\left(\left\{|\phi_{i,j}-\widehat{\phi}_k|^2\middle|k\right\}, A_{\text{th}}^2\right), \tag{18}$$

where A_{th} is a constant threshold, and $|\Phi_i|$ denotes the cardinality of the set Φ_i. Then the estimated position with the measured AoA profile $\widehat{\Phi}$ can be obtained by finding the position with the smallest value of the error function out of all feasible positions in the reconstructed layout.

$$i^\star = \arg\min_{i\in\mathscr{G}} f(\Phi_i,\widehat{\Phi}). \tag{19}$$

As a remark notice that the threshold A_{th} in (18) is to avoid a significant difference in the error function when the desired LoS and first-order reflection paths are blocked, or higher-order reflection paths are captured in the AoA detection.

VI. Experiment and Discussion

A. *mmReality System Implementation*

The block diagram of mmReality is illustrated in Fig. 4. Taking the transmitter side as an example, one software-defined radio (SDR) generates the baseband signal and up-converts it to the intermediate frequency (IF) band centered at 500 MHz. The IF signal is fed into 90° and 180° power splitters sequentially to generate differential in-phase and quadrature (IQ) signals. Then the IF signal is further up-converted to 60 GHz and finally transmitted by a 16-antenna phased array. The antenna selection, beam switch, and power gain of the phased array are controlled by a host computer. To achieve sufficient ranging accuracy, the transmission signal is modulated with 8 subcarriers and 12.5 MHz bandwidth via OFDM technology.

Before the measurements, the inter-element spacing and the inter-element phase offset of both phased arrays at the transmitter and the receiver should be calibrated, which is elaborated below.

Inter-element spacing calibration: Although antenna arrays are designed with half-wavelength inter-element spacing to generate beam patterns with a single main lobe and low side lobes, the wavelength varies at different carrier frequencies. The difference of adjacent carrier frequencies in the 60 GHz band is generally more than 1 GHz and cannot be neglected. Moreover, the direct measurement of inter-element spacing may not be accurate due to the short wavelength and small antenna size[19].

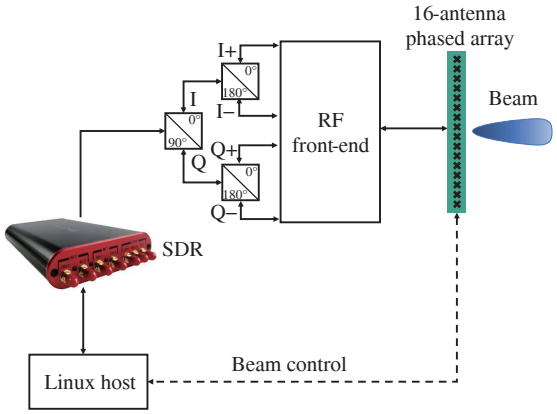

Fig. 4 Hardware architecture

To address the above issue, we measure the inter-element spacing via the received signals of the phased array. We use a transmitter with a horn antenna to transmit a single tone and mount the phased array to be calibrated on a rotation platform as the receiver. The mmWave absorbers are used to suppress the potential NLoS paths. The received signals are collected at N_θ different AoAs. For a certain AoA, each antenna element is triggered alternatively to receive the same single tone. Let $\varphi_{m,n}$ be the estimated phase of the nth antenna element at the mth AoA, denoted as θ_m, then the inter-element spacing can be estimated by

$$d^\star = \arg\max_d \sum_{n=2}^{N} \left| \sum_{m=1}^{N_\theta} \exp\left(\mathrm{j}\left(\varphi_{m,n} - \varphi_{m,n-1} - 2\pi \frac{d \sin\theta_m}{\lambda} \right) \right) \right|. \tag{20}$$

Inter-element phase offset calibration: Notice that the phase offset is caused by the different transmission lines of antenna elements, we calibrate it with a transmitter at the boresight direction of the phased array. In the above calibration of inter-element spacing, let $\theta_1 = 0$, the phase offset difference of two adjacent elements (say between the nth and $(n-1)$th antenna elements) due to transmission lines can be estimated directly by $\varphi_{1,n} - \varphi_{1,n-1}$. As a result, the phase offset of all the remaining antenna elements with respect to the first element can be compensated.

The mmReality system is deployed in a corridor with an irregular layout as illustrated in Fig. 5. The position of the transmitter is fixed, and the receiver is put at 15 measurement points respectively as in Fig. 8. At each measurement point, the OFDM signal is transmitted via 16×16 pairs of transmission and receiving beams.

B. Accuracy of AoA/AoD Estimation

In this part, the accuracy of AoA and AoD estimations based on the MUSIC algorithm is illustrated. The estimated AoAs/AoDs and the ground truths for LoS paths and NLoS paths (first-order reflection paths) are illustrated in Fig. 6(a) and Fig. 6(c), respectively. The ground truth AoAs/AoDs in the environment is measured by a laser rangefinder. Since the AoA/AoD in 360° azimuth can be estimated by rotating the phased array towards the four quadrants, we only estimate the angles ranging from −45° to 45°. It can be observed that the estimated AoAs/AoDs match the ground truth in both LoS and NLoS scenarios. Moreover, the cumulative distribution functions (CDF) of the magnitudes of the estimation errors for the LoS scenario and the NLoS scenario are illustrated in Fig. 6(b) and Fig. 6(d), respectively. It can be observed that 90% of the estimations are with estimation errors less than 4°.

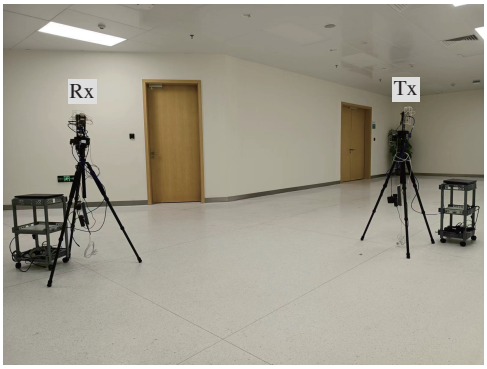

Fig. 5 Experimental environment of the corridor

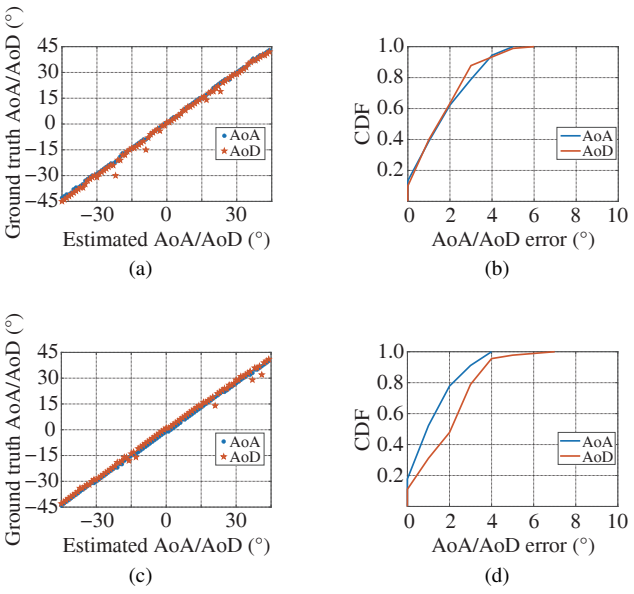

Fig. 6 Illustration of AoA/AoD estimation: (a) Estimated AoA/AoD versus ground truth in LoS scenario; (b) CDF of AoA/AoD estimation error in LoS scenario; (c) Estimated AoA/AoD versus ground truth in NLoS scenario; (d) CDF of AoA/AoD estimation error in NLoS scenario

C. Accuracy of Path Length Estimation

Fig. 7(a) and Fig. 7(c) illustrate the estimated path lengths and the ground truth for LoS paths and NLoS paths (first-order reflection paths), respectively. The estimated path lengths range from 1.6 m to 10 m for a typical indoor scenario. It can

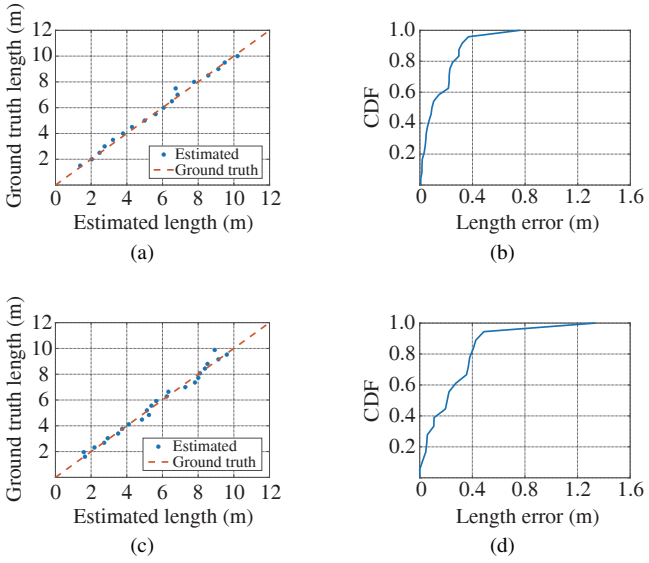

Fig. 7 Illustration of path length estimation: (a) Estimated path length versus ground truth in LoS scenario; (b) CDF of the estimation error of path lengths in LoS scenario; (c) Estimated path length versus ground truth in NLoS scenario; (d) CDF of the estimation error of path lengths in NLoS scenario

be observed that the estimated path lengths match the ground truths in both LoS and NLoS scenarios. The CDFs of the path length estimation errors for LoS paths and NLoS paths are illustrated in Fig. 7(b) and Fig. 7(d), respectively, where the average estimation error for LoS paths and NLoS paths are 0.15 m and 0.25 m, respectively. It is intuitive that the estimation for LoS paths performs better than that for NLoS paths because NLoS paths suffer severe reflection loss.

D. Room Layout Reconstruction

Integrating the estimated AoAs, AoDs, and path lengths at all measurement points, the reconstructed layout of the corridor is illustrated in Fig. 9, where the blue solid line and the red dotted line represent the real and estimated walls, respectively. It can be seen that all six walls are detected with high estimation accuracy, as both lines almost overlap. Moreover, the estimated positions of measurement points, virtual transmitters, and reflecting points are also illustrated in Fig. 9. As a remark notice that higher-order reflections can be found in the measurements, although the LoS and first-order reflection paths are dominant. However, since the virtual transmitters of the higher-order reflection paths are sparse, they are eliminated by the DBSCAN algorithm. Hence, only the estimated virtual transmitter positions of the first-order reflection is shown in Fig. 9.

The CDFs of the localization errors of the measurement points and reflection points are illustrated in Fig. 10(a) and Fig. 10(b), respectively. The average localization error of the measurement points is 0.42 m, and 90% of the localization

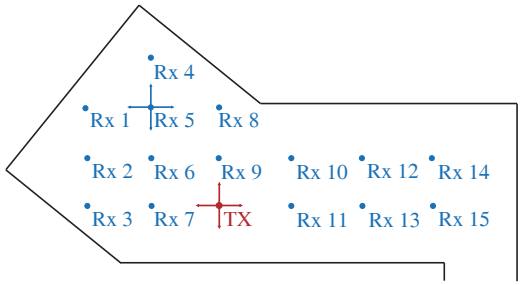

Fig. 8 Corridor layout illustration with the positions of the transmitter and measurement points

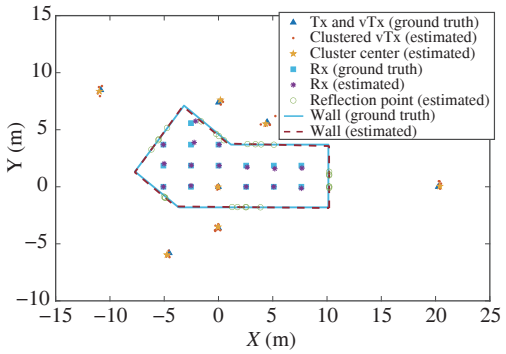

Fig. 9 Corridor layout reconstruction

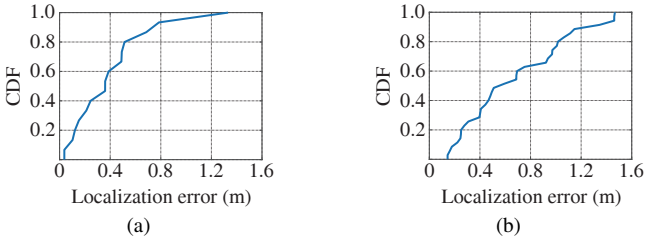

Fig. 10 CDF of the localization error: (a) Measurement points; (b) Reflection points

errors are below 0.8 m, while those of the estimated reflection points are 0.6 m and 1.2 m respectively. The localization error of reflection points is generally larger. This is because the localization of reflection points is based on the estimated positions of measurement points.

E. Localization Accuracy via AoA Spectrum

Based on the detected corridor layout, the localization performance via the AoA spectrum is demonstrated in this part. Specifically, the receiver is randomly deployed at 25 positions in the corridor successively, and the AoA spectrum is measured by the receiver at each position for localization. The CDF of localization error is illustrated in Fig. 11. It can be observed that 90% of the localization error is within 1.3 m, and the average localization error is 1.0 m. Two examples of localization via AoA spectrum are shown in Fig. 12, where different colors are used to demonstrate the value of the er-

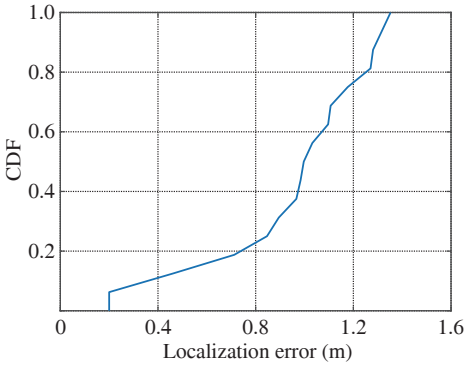

Fig. 11 CDF of the localization error based on the reconstructed layout and measurements of AoA spectrum

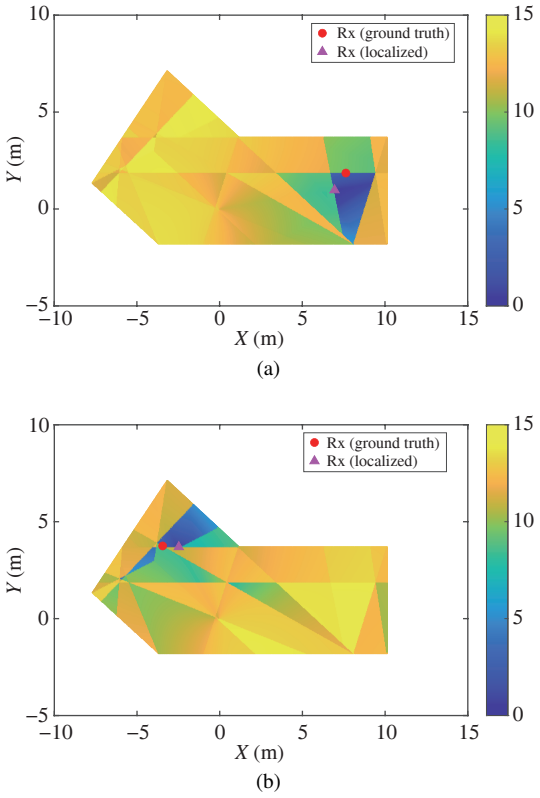

Fig. 12 Two examples of localization via AoA spectrum

ror function f defined in (18). The localization error mainly results from the localization error of virtual transmitters.

F. Impact of Measurement Point Number

We evaluate the impact of the number of measurement points on the localization accuracy in another indoor environment as illustrated in Fig. 13(a). The detection accuracy of the marked wall (as well as the virtual transmitter via the wall) is evaluated. As shown in Fig. 13(b), the transmitter is deployed 4.06 meters away from the wall and 21 points between the transmitter and the wall are taken as the candidate measurement points. The localization accuracy of the virtual transmitter versus the number of measurement points is shown in Fig. 14. For a given number, the measurement points are randomly picked from the 21 candidates 100 times for averaging. It can be observed that with more than 16 measurement points, the localization error can converge to 0.26 m.

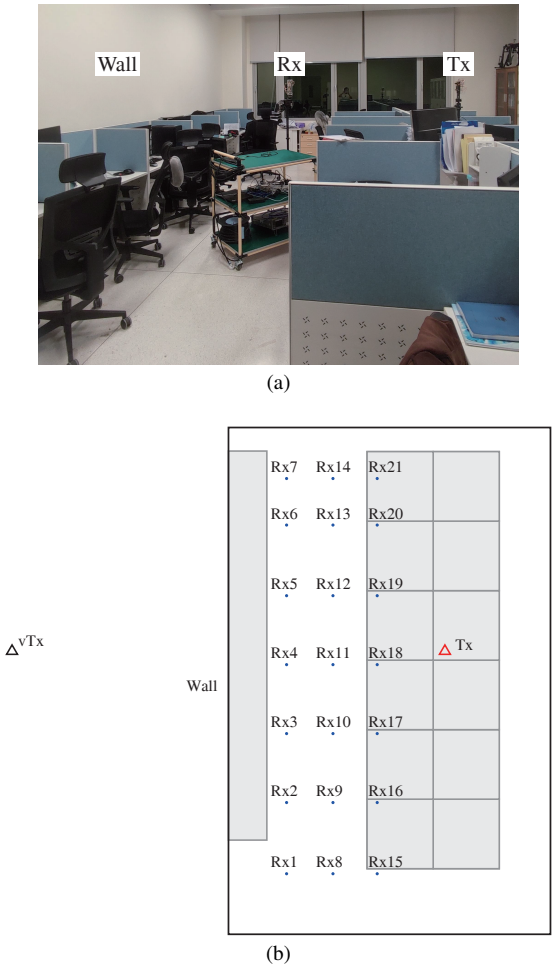

Fig. 13 (a) Experimental environment of the office; (b) Office layout and the positions of the transmitter and measurement points

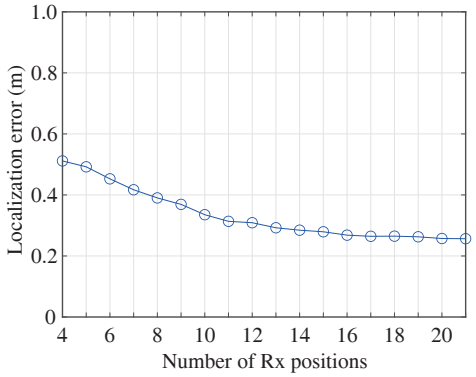

Fig. 14 Localization error versus the number of measurement positions

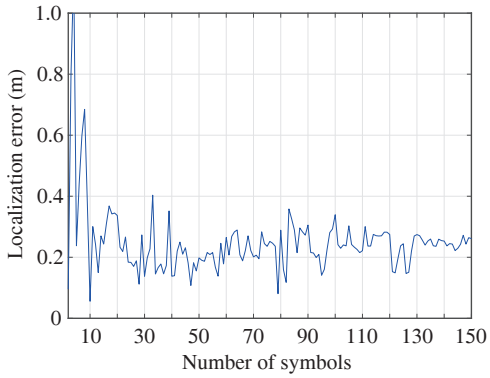

Fig. 15 Localization error versus the number of received OFDM symbols

G. Impact of Measurement Time

We then analyze the sensitivity of the virtual transmitter localization with respect to the measurement time, i.e., the number of received OFDM symbols for each pair of precoder and combiner. As shown in Fig. 15, the number of received OFDM symbols will affect the accuracies of both angle and path length estimation, and finally the estimated position of the virtual transmitter. The localization error decreases significantly with the OFDM symbol number at the very beginning. With more than 40 received OFDM symbols, the localization error of the virtual transmitter will be below 0.4 m. Note that it takes around 13.1 ms to transmit 40 OFDM symbols for all the pairs of precoder and combiner.

VII. Conclusion

In this paper, the mmReality system for indoor layout reconstruction and fast localization was elaborated. Exploiting the quasi-statistic channel, the 2D-MUSIC algorithm was used to detect the AoAs and AoDs of the paths between the transmitter and the receiver with an analog MIMO front-end. The path length can then be estimated via multi-carrier ranging. Based on the AoAs, AoDs, and path lengths estimated by the receiver at different locations, the indoor layout can be reconstructed. With the layout knowledge, we continue to show that the receiver can be localized via the observed AoAs. The experiment results of this paper demonstrated the feasibility to track the environment and trajectory of mobile devices via mmWave communication signals. With both environment and trajectory information, communication efficiency may be improved, which is a promising topic for future study.

In our current testbed, the mmWave RF front-end support IEEE 802.11ad communication, i.e., gigahertz bandwidth. However, due to the limited sampling rate of the baseband processor and throughput of the network interface card, we can only apply 12.5 MHz bandwidth at 60 GHz for wireless sensing. The limited bandwidth in the baseband results in low-range resolution (12 meters for 12.5 MHz bandwidth) for room layout reconstruction. The system design supporting gigahertz-bandwidth mmWave communications and sensing is left for future work.

References

[1] ZHU Y, ZHU Y, ZHAO B Y, et al. Reusing 60GHz radios for mobile radar imaging[C]//Proceedings of the 21st Annual International Conference on Mobile Computing and Networking. New York: The Association for Computing Machinery, 2015: 103-116.

[2] BARNETO C B, RASTORGUEVA-FOI E, KESKIN M F, et al. Millimeter-wave mobile sensing and environment mapping: models, algorithms and validation[J]. IEEE Transactions on Vehicular Technology, 2022, 71(4): 3900-3916.

[3] WEI T, ZHOU A, ZHANG X. Facilitating robust 60 GHz network deployment by sensing ambient reflectors[C]//Proceedings of 14th USENIX Symposium on Networked Systems Design and Implementation. Berkeley: USENIX Association, 2017: 213-226.

[4] BAHL P, PADMANABHAN V N. RADAR: an in-building RF-based user location and tracking system[C]//Proceedings of 19th Annual Joint Conference of the IEEE Computer and Communications Societies. Piscataway: IEEE Press, 2000: 775-784.

[5] YOUSSEF M, AGRAWALA A. The Horus WLAN location determination system[C]//Proceedings of the 3rd International Conference on Mobile Systems, Applications, and Services. New York: The Association for Computing Machinery, 2005: 205-218.

[6] WANG X, GAO L, MAO S, et al. CSI-based fingerprinting for indoor localization: a deep learning approach[J]. IEEE Transactions on Vehicular Technology, 2016, 66(1): 763-776.

[7] KOIKE-AKINO T, WANG P, PAJOVIC M, et al. Fingerprinting-based indoor localization with commercial mmWave Wi-Fi: a deep learning approach[J]. IEEE Access, 2020, 8: 84879-84892.

[8] XIONG J, JAMIESON K. ARRAYTRACK: a fine-grained indoor location system[C]//Proceedings of 10th USENIX Symposium on Networked Systems Design and Implementation. Berkeley: USENIX Association, 2013: 71-84.

[9] KOTARU M, JOSHI K, BHARADIA D, et al. Spotfi: decimeter level localization using Wi-Fi[C]//Proceedings of the 2015 ACM Conference on Special Interest Group on Data Communication. New York: The Association for Computing Machinery, 2015: 269-282.

[10] GJENGSET J, XIONG J, MCPHILLIPS G, et al. Phaser: enabling phased array signal processing on commodity Wi-Fi access points[C]//Proceedings of the 20th Annual International Conference on Mobile Computing and Networking. New York: The Association for Computing Machinery, 2014: 153-164.

[11] VASISHT D, KUMAR S, KATABI D. Decimeter-level localization with a single Wi-Fi access point[C]//Proceedings of 13th USENIX Symposium on Networked Systems Design and Implementation. Berkeley: USENIX Association, 2016: 165-178.

[12] XIONG J, SUNDARESAN K, JAMIESON K. ToneTrack: leveraging frequency-agile radios for time-based indoor wireless localization[C]//Proceedings of the 21st Annual International Conference on Mobile Computing and Networking. New York: The Association for Computing Machinery, 2015: 537-549.

[13] CHEN Z, ZHU G, WANG S, et al. M^3M3: multipath assisted Wi-Fi localization with a single access point[J]. IEEE Transactions on Mobile Computing, 2019, 20(2): 588-602.

[14] SOLTANAGHAEI E, KALYANARAMAN A, WHITEHOUSE K. Multipath triangulation: decimeter-level Wi-Fi localization and orientation with a single unaided receiver[C]//Proceedings of the 16th Annual International Conference on Mobile Systems, Applications,

and Services. New York: The Association for Computing Machinery, 2018: 376-388.

[15] WANG J, LAN Z, SUM C S, et al. Beamforming codebook design and performance evaluation for 60GHz wideband WPANs[C]//Proceedings of 2009 IEEE 70th Vehicular Technology Conference Fall. Piscataway: IEEE Press, 2009: 1-6.

[16] YEH C C, LEE J H, CHEN Y M. Estimating two-dimensional angles of arrival in coherent source environment[J]. IEEE Transactions on Acoustics, Speech, and Signal Processing, 1989, 37(1): 153-155.

[17] GUAN J, PAIDIMARRI A, VALDES-GARCIA A, et al. 3-D imaging using millimeter-wave 5G signal reflections[J]. IEEE Transactions on Microwave Theory and Techniques, 2021, 69(6): 2936-2948.

[18] ESTER M, KRIEGEL H P, SANDER J, et al. A density-based algorithm for discovering clusters in large spatial databases with noise[C]//Proceedings of the Second International Conference on Knowledge Discovery and Data Mining. Berlin: Springer, 1996: 226-231.

[19] AYYALASOMAYAJULA R, ARUN A, WU C, et al. LocAP: autonomous millimeter accurate mapping of Wi-Fi infrastructure[C]//Proceedings of 17th USENIX Symposium on Networked Systems Design and Implementation. Berkeley: USENIX Association, 2020: 1115-1129.

About the Authors

Yifei Sun (Graduate Student Member, IEEE) received the B.E. degree in Communication Engineering from Southern University of Science and Technology (SUSTech), Shenzhen, China, in 2019. He is currently pursuing the Ph.D. degree with the Department of Computer Science, the University of Hong Kong (HKU), Hong Kong, China. His research interests include integrated sensing and communication (ISAC) and wireless radio resource management.

Jie Li received the B.Eng. and M.Eng. degrees from the Southern University of Science and Technology (SUSTech), Shenzhen, China, in 2019 and 2022, respectively. He is currently a software engineer with Tencent. His research interests include integrated sensing and communication (ISAC) and passive sensing.

Tong Zhang (Member, IEEE) received the B.S. degree from Northwest University (NWU), Xi'an, China, in 2012, the M.S. degree from Beijing University of Posts and Telecommunications (BUPT), Beijing, China, in 2015, and the Ph.D. degree in Electronic Engineering from the Chinese University of Hong Kong (CUHK), Hong Kong, China, in 2020. He is currently a Postdoc Fellow at Southern University of Science and Technology (SUSTech), Shenzhen, China. He received the 31st Wireless and Optical Communications Conference (WOCC 2022) Charles Kao Best Paper Award.

Rui Wang [corresponding author] (Member, IEEE) received the B.S. degree from University of Science and Technology of China, Hefei, China, in 2004 and the Ph.D. degree in Wireless Communications from the Hong Kong University of Science and Technology, Hong Kong, China, in 2008. From 2009 to 2012, he was a Senior Research Engineer with Huawei Technologies Company Ltd., Shenzhen, China. Since 2012, he has been with Southern University of Science and Technology, Shenzhen, China, as an Associate Professor. He has research experience in both academia and industry. He has authored over 100 papers in top-level IEEE journals and flagship international conferences, especially in the area of wireless radio resource optimization and interference management. He has contributed to over 20 U.S. patent applications and over 30 Chinese patent applications (20 of them have been granted). He also involved in the development of interference mitigation technology for 5G systems.

Xiaohui Peng (Member, IEEE) received the B.S. degree in Electronic and Information Engineering from Zhengzhou University, Zhengzhou, China, in 2012, and the Ph.D. degree in Electronic Science and Technology from Huazhong University of Science and Technology, Wuhan, China, in 2018. He is a Senior Engineer with Huawei Technologies Company Ltd., Shenzhen, China. His research interests include array signal processing and passive microwave remote sensing, with special emphasis on synthetic aperture interferometric radiometers.

Xiao Han (Senior Member, IEEE) is currently a Principal Engineer with Huawei Technologies Co., Ltd., Shenzhen, China. He received the B.E. degree in Electrical Engineering from Sichuan University, Chengdu, China, and the Ph.D. degree in Communication Engineering from Zhejiang University, Hangzhou, China. He was a Post-Doctoral Research Fellow with the National University of Singapore.

He was the Chair of IEEE 802.11 WLAN Sensing Topic Interest Group (TIG), the Chair of 802.11 WLAN Sensing Study Group (SG), and currently he is serving as the Chair of IEEE 802.11bf WLAN Sensing Task Group (TG). He is the Industry Chair of IEEE ComSoc Integrated Sensing and Communication Emerging Technology Initiative (ISAC-ETI), the Vice Chair of IEEE WTC Special Interest Group (SIG) on ISAC, a Guest Editor of the IEEE Journal on Selected Areas in Communications (JSAC) Special Issue on "Integrated Sensing and Communications (ISAC)", and he has served as the ISAC Workshop Co-Chair of IEEE GLOBECOM 2020. His research interests include wireless communication, signal processing, integrated sensing and communication (ISAC), and standardization of wireless communication.

Haisheng Tan (Senior Member, IEEE) received the B.E. degree in Software Engineering and the B.S. degree in Management both from University of Science and Technology of China (USTC), Hefei, China, with the highest honor. Then, he got the Ph.D. degree in Computer Science at the University of Hong Kong (HKU), Hong Kong, China. He is currently a Professor at USTC, Hefei, China. His research interests include algorithms and networking. Dr. Tan has published over 80 papers in prestigious journals and conferences, mainly in the areas of AIoT and edge computing. He recently received the Best Paper Award in WASA'19, CWSN'20, PDCAT'20, and ICAPDS'21.